AFRL-SR-AR-TR-03-

0510

REPORT DOCUMENTATION PAGE

1. AGENCY USE ONLY (Leave blank)	2. REPORT DATE	3. REPORT TYPE AND DATES COVERED
	11/30/2003	Final From 06/1/01 to 11/30/03

4. TITLE AND SUBTITLE
Localized Flow Control in High Speed Flows Using Laser Energy Deposition

5. FUNDING NUMBERS
F49620-01-1-0368

6. AUTHOR(S)
Doyle Knight, Hong Yan Greg Elliott
Graham Candler Alexander Zheltovodov

7. PERFORMING ORGANIZATION NAME(S) AND ADDRESS(ES)
Department of Mechanical and Aerospace Engineering
Rutgers University
98 Brett Road
Piscataway, NJ 08854-8058

8. PERFORMING ORGANIZATION REPORT NUMBER
Report CCD 2003-25

9. SPONSORING / MONITORING AGENCY NAME(S) AND ADDRESS(ES)
Air Force Office of Scientific Research
AFOSR/NM
801 N. Randolph St., Rm 732
Arlington, VA 22203-1977

10. SPONSORING / MONITORING AGENCY REPORT NUMBER

11. SUPPLEMENTARY NOTES

12a. DISTRIBUTION / AVAILABILITY STATEMENT
Unclassified Distribution Unlimited

12b. DISTRIBUTION CODE

13. ABSTRACT *(Maximum 200 Words)*

The capability for localized flow control in high speed flows using laser energy deposition has been investigated in a collaborative computational and experimental program. Three proposed applications have been comprehensively studied. First, two models of laser energy deposition in air have been developed and validated by comparison with experiment. The first model is an engineering approach wherein the laser energy deposition is treated as an energy release in a perfect gas. The second model is a detailed physical approach which incorporates real gas chemistry with an eleven species model of air. Comparison with experimental measurements of static temperature, density and velocity (one-component) show good agreement with both models outside the plasma region. Second, a detailed 3-D simulation of laser energy deposition upstream of intersecting shocks at Mach 3.45 demonstrated the capability to force transition from Mach Reflection (MR) to Regular Reflection (RR) in the Dual Solution Domain. This result is particularly important for control of MR to RR transition in high speed inlets for scramjet-powered air vehicles. A companion experimental study showed a momentary reduction in the Mach stem height by 70%, but a Mach Reflection was recovered apparently due to freestream turbulence. Third, detailed 3-D simulations of laser energy deposition upstream of an isolated sphere and an Edney IV interaction at Mach 3.45 were performed. Results show the fundamental features observed in the accompanying experiments.

14. SUBJECT TERMS
Local flow control, Energy deposition

15. NUMBER OF PAGES
23

16. PRICE CODE

17. SECURITY CLASSIFICATION OF REPORT	18. SECURITY CLASSIFICATION OF THIS PAGE	19. SECURITY CLASSIFICATION OF ABSTRACT	20. LIMITATION OF ABSTRACT
Unclassified	Unclassified	Unclassified	

Localized Flow Control in High Speed Flows Using Laser Energy Deposition

Doyle D. Knight and Hong Yan
Dept of Mechanical and Aerospace Engineering
Rutgers – The State University of New Jersey
98 Brett Road, Piscataway, NJ 08854-8058
Phone: 732 445 4464 · Cellphone: 732 762 5510
Faxsimile: 732 445 4464 · Email: ddknight@rci.rutgers.edu

Greg Elliott
Department of Aeronautical and Astronautical Engineering
University of Illinois at Urbana-Champaign
Urbana, IL 61801

Prof. Graham Candler
Department of Aerospace Engineering and Mechanics
University of Minnesota
107 Akerman Hall
110 Union Street SE, Minneapolis, MN 55455
Phone: 612 625 2364 · Fax: 612 626 1558
Email: candler@aem.umn.edu

Dr. Alexander Zheltovodov
Institute of Theoretical and Applied Mechanics
Siberian Branch of the Russian Academy of Sciences
Institutskaya St., 4/1, Novosibirsk 630090, Russia
Phone: 011 7 3832 30 3430 · Fax: 011 7 3832 34 2268
Email: zhelt@itam.nsc.ru

Final Technical Report
1 June 01 - 30 November 03

AFOSR Grant F49620-01-1-0368

Submitted to
Dr. John Schmisseur
AFOSR/NM
801 N. Randolph St., Rm 732
Arlington, VA 22203-1977

30 Nov 2003

Abstract

The capability for localized flow control in high speed flows using laser energy deposition has been investigated in a collaborative computational and experimental program. Three proposed applications have been comprehensively studied. First, two models of laser energy deposition in air have been developed and validated by comparison with experiment. The first model is an engineering approach wherein the laser energy deposition is treated as an energy release in a perfect gas. The second model is a detailed physical approach which incorporates real gas chemistry with an eleven species model of air. Comparison with experimental measurements of static temperature, density and velocity (one-component) show good agreement with both models outside the plasma region. Second, a detailed 3-D simulation of laser energy deposition upstream of intersecting shocks at Mach 3.45 demonstrated the capability to force transition from Mach Reflection (MR) to Regular Reflection (RR) in the Dual Solution Domain. This result is particularly important for control of MR to RR transition in high speed inlets for scramjet-powered air vehicles. A companion experimental study showed a momentary reduction in the Mach stem height by 70%, but a Mach Reflection was recovered apparently due to freestream turbulence. Third, detailed 3-D simulations of laser energy deposition upstream of an isolated sphere and an Edney IV interaction at Mach 3.45 were performed. Results show the fundamental features observed in the accompanying experiments.

Contents

1 Introduction

The aerodynamic performance of high speed (*i.e.*, supersonic and hypersonic) vehicles is often controlled by *highly localized* fluid dynamic phenomena. For example, the supersonic jet formed in an Edney IV shock-shock interaction at hypersonic speeds can increase peak surface heat transfer by several orders of magnitude [1]. A hypersonic vehicle would naturally be designed to avoid such a potentially disasterous situation to the maximum extent possible (and most certainly at its cruise condition). Nevertheless, the thermal protection system must allow for such extraordinary *local* anomalous behavior, even if such behavior occurs only momentarily during maneuver or gust response. Thus, a *local* (both in space and in time) fluid dynamic phenomenon can affect the *global* vehicle design.

Laser energy deposition is a promising technique for *localized* flow control for supersonic and hypersonic vehicles. Pilyugin *et al* [2] surveyed modern studies of supersonic flows with physical-chemical heterogeneity including different applications of laser energy deposition. These studies show that laser energy addition strongly affects the shock waves and flowfield structures and can be used for flow control in a variety of aerodynamic applications. For example, heat addition close to a vehicle's surface can cause the appearance of regions of increased or decreased pressure which can be employed to improve the vehicle's aerodynamic performance. Also, a body immersed in a wake with high level of the total pressure losses downstream of the laser induced-energy source can experience significant drag reduction. Tretyakov *et al* [3] achieved a 40% reduction in drag on spherical and conical bodies using pulsed laser energy deposition. Levin and Terent'eva [4] obtained up to 30% increase in lift on a cone by continuous energy deposition above the cone surface. Riggins *et al* [5] demonstrated a 30 to 50% drag reduction on a blunt body at Mach 6.5 and 10.

While many recent experimental and computational studies of energy deposition in supersonic and hypersonic flows have concerned *global* vehicle aerodynamics, Our combined computational and experimental research program focused on *local* control of supersonic and hypersonic flows by laser energy deposition. The application of the techniques developed in this research would involve *small scale* energy deposition systems on flight vehicles, as opposed to the large scale energy sources required for global flow control, and therefore could be a feasible concept for current and future air vehicles.

This report summarizes the research activities on locally controlling high speed flows using laser energy deposition. Results for three applications will be presented.

2 Methodology

2.1 Experiment Achievements

Two advances in experimental diagnostics were achieved during the course of the experimental investigation into energy deposition in supersonic flows. The first advance was the further development and application of Filtered Rayleigh Scattering (FRS) to obtain measurement of multiple properties. Prof. Elliott and his research group have developed molecular filtered based diagnostics (including those associated with FRS) with funding from the National Science Foundation. During the current research program, Prof. Elliott's research group has applied and developed FRS for analyzing the flow field associated with laser induced breakdown in air including new methods of calibration (correcting for sources of noise, background scattering and variations in laser frequency)

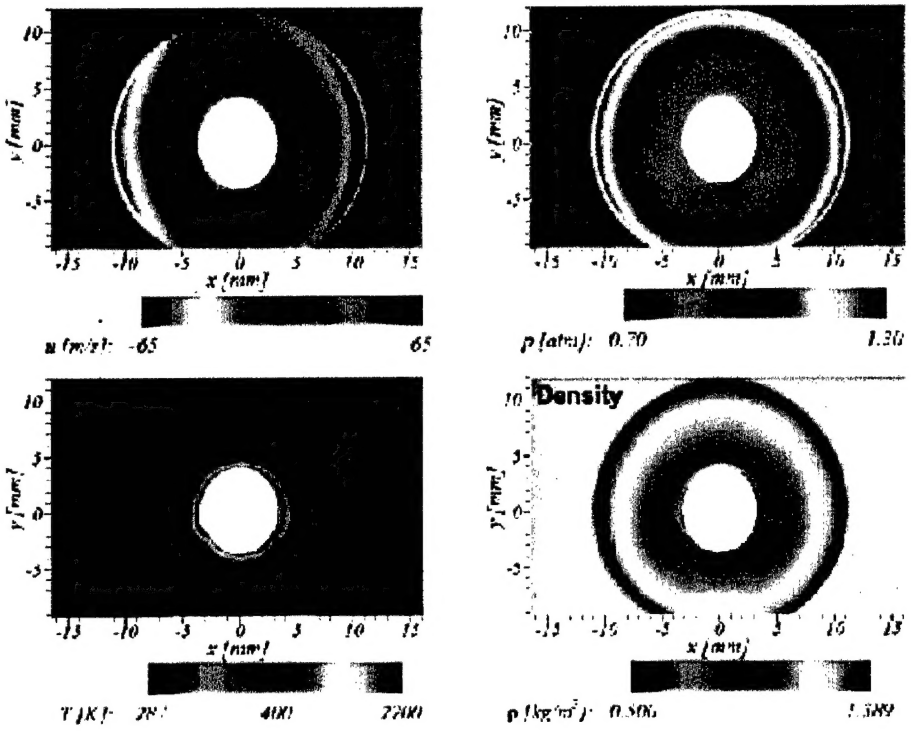

Figure 1: FRS measurement of velocity, pressure, temperature and density ($t = 20$ μs, $E = 145$ mJ)

and improved user friendly menu driven data analysis routines that enable rapid evaluation of experimental data.

Fig. 1 shows images of the pressure, density, temperature and horizontal component of the velocity of the flowfield created by laser induced breakdown in quiescent air. The increase in the pressure, temperature, density, and velocity is clearly evident and agrees well with the computational models developed in this study (see Section 3.1). Assuming that the pressure is approximately constant at later times (a result substantiated by simulations), instantaneous temperature measurements can be made of the vortex ring that is a principle feature of the flow at later times. Fig. 2 displays the temporal evolution of the temperature field (taken in the plane of symmetry of the energy deposition) for laser induced breakdown in quiescent air for $E = 145$ mJ. The laser beam is incident vertically downwards. Several prominent flow features are evident including the vortex ring, the jet structure induced by the vortex ring, and the diffusive cooling of the vortex ring and jet.

The second advance in experimental diagnostics is the development of a new broadband source for use in schlieren photography. Schlieren was utilized in several of the studies of the various supersonic flows which were investigated to study the influence of laser energy perturbations to the shock structure. One problem that was encountered was the lack of a good light source that had a small pulse width and accurate timing. The xenon flashlamp utilized previously had a pulse width of a few microseconds and had a significant jitter in the timing with the input signal. A laser is not an ideal light source for schlieren photography because laser speckle generates noise and diffraction fringes at the knife edge. The new technique uses a Nd:YAG (532 nm wavelength) laser beam focused and discharged onto a 2% thoriated tungsten rod in an argon flow to generate the schlieren light source (Fig. 3). In order to improve the intensity collimated onto the first mirror

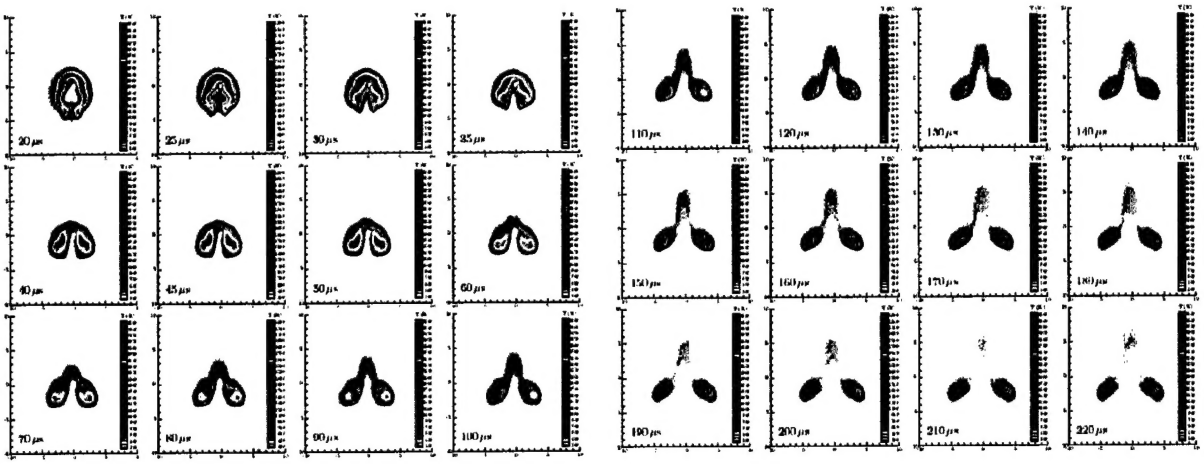

Figure 2: Time sequence of FRS temperature measurement ($E = 145$ mJ)

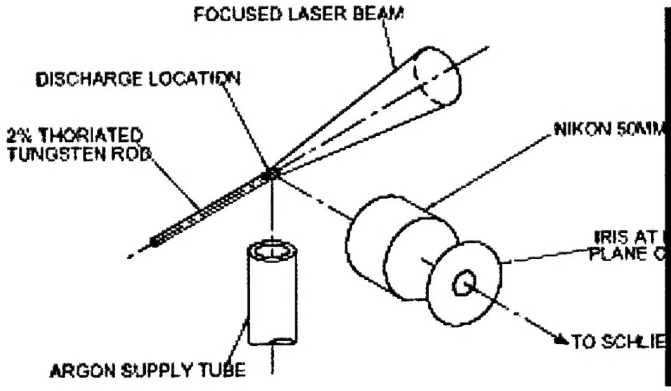

Figure 3: Laser-argon spark source

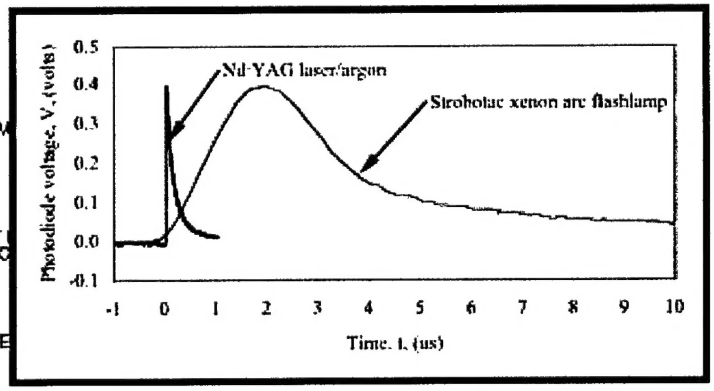

Figure 4: Pulse width comparison

in the schlieren system, a lens pin hole combination is utilized. Fig. 4 compares the pulse width measured with a photodiode for the xenon Stobotac flash lamp and the laser/argon flash source. The half-peak pulse width for the Nd:YAG discharge in argon is 0.12 μs compared to 2 μs for the xenon flash lamp. Fig. 5 compares the two flash sources for a laser discharge in quiescent air next to a 25.4 mm sphere. The schlieren image for the Nd:YAG discharge in argon (Fig. 5(b)) is clearly superior to the image for the xenon flash lamp (Fig. 5(a)). The increase in image quality is due to 1) the decreased pulse width of the flash source (leading to sharper images of moving events), 2) the ability to filter the light emitted from the laser energy deposition spark, and 3) the ability to control the jitter of the light source when it is time synced with the laser discharge. Since the Nd:YAG discharge in argon is driven by the laser, its time can be controlled within 10 ns to the laser used for the laser energy deposition discharge. The xenon Strobotac light source can only be controlled within 2 μs when synchronized in time with the discharge laser. Therefore, phase-locked images produced by the Nd:YAG discharge in argon have three orders of magnitude less variation when compared to phase-locked images produced with the xenon Strobotac light source.

In addition, we obtained significant experience in the fabrication and use of thin film metallic heat transfer gauges during the research program. Although the gauges and associated electronics do not

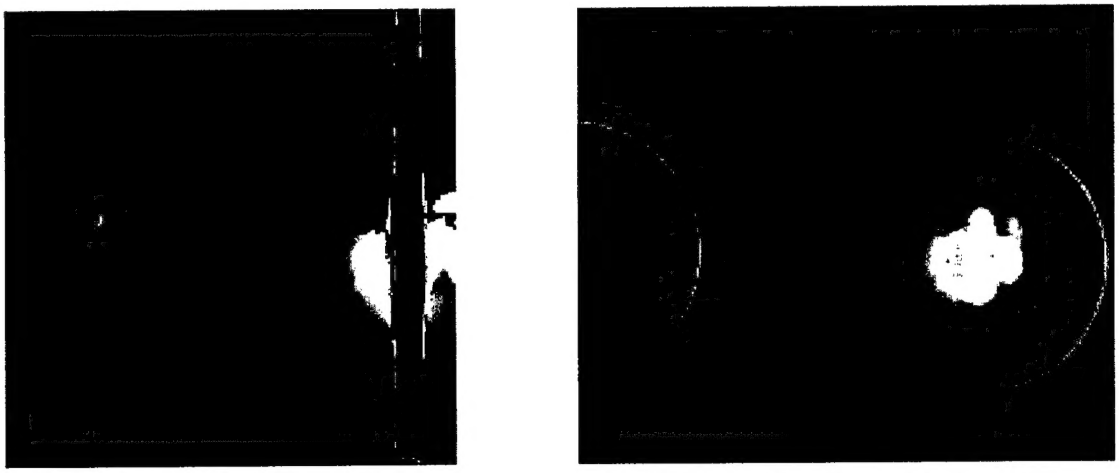

(a) Strobotac flash source (b) Nd:YAG in argon flash source

Figure 5: Comparison of flash sources for schlieren image of laser energy deposition

represent a new experimental diagnostic, this experience has extended our diagnostic capability. The heat transfer gauges were used to assess the effect of laser energy deposition on surface heat transfer for an isolated sphere and an Edney IV interaction at Mach 3.45. The gauge fabrication and calibration technique, and results for the isolated sphere and Edney IV interaction are described in Adelgren *et al* [6] and Adelgren [7].

2.2 Numerical Methodology

Two different versions of the perfect gas model were used. The first version assumes one-dimensional spherically symmetric flow and was used for simulation of laser energy deposition in quiescent air (section 3.1). The second version used the GASPex code [8] for fully three-dimensional flow. The one-dimensional model is described herein. Details of the GASPex code are presented in [8]

We have utilized two different models for laser energy deposition in a gas. The first model assumes a perfect gas and parameterizes the energy deposition in a simple manner. A specified fraction ϵ_E of the laser energy pulse is assumed to be absorbed by the gas and a Gaussian initial distribution for temperature and pressure is utilized. Model details are presented in Yan *et al* [9]. This approach requires experimental data (*e.g.*, blast wave radius *vs* time) for calibration of ϵ_E which depends on laser wavelength, pulse energy and duration. The principle advantage of this model is simplicity, *i.e.*, the laser energy pulse constitutes an initial condition to an otherwise perfect gas simulation. This approach allowed us to perform simulations of laser energy deposition early on in our research program while the more detailed (and physically realistic) second model was being developed. Results of the first model are described in Section 3.1.

The one-dimensional time-dependent compressible Navier-Stokes equations in the spherical polar coordinate system can be written as

$$\frac{\partial \rho}{\partial t} + \frac{\partial(\rho v_r)}{\partial r} + \frac{2\rho v_r}{r} = 0 \tag{1}$$

$$\frac{\partial \rho v_r}{\partial t} + \frac{\partial(\rho v_r^2 + p)}{\partial r} + \frac{2\rho v_r^2}{r} = \frac{4}{3}\frac{\partial}{\partial r}[\mu(\frac{\partial v_r}{\partial r} - \frac{v_r}{r})] + \frac{4\mu}{r}(\frac{\partial v_r}{\partial r} - \frac{v_r}{r}) \tag{2}$$

$$\frac{\partial \rho e}{\partial t}+\frac{\partial(\rho e v_r+p v_r)}{\partial r}+\frac{2(\rho e v_r+p v_r)}{r}=\frac{4}{3}\frac{\partial}{\partial r}[\mu v_r(\frac{\partial v_r}{\partial r}-\frac{v_r}{r})]+\frac{8}{3}\mu\frac{v_r}{r}(\frac{\partial v_r}{\partial r}-\frac{v_r}{r})+\frac{\partial}{\partial r}(\kappa_e\frac{\partial T}{\partial r})+\frac{2}{r}\kappa_e\frac{\partial T}{\partial r} \tag{3}$$

The state equation of ideal gas is

$$p=\rho RT \tag{4}$$

where

$$\kappa_e=\kappa+\frac{16}{3}\frac{\sigma_s}{\alpha_R}T^3 \tag{5}$$

The dynamic viscosity μ using Sutherland's law is calculated as follows

$$\mu=\mu_{ref}(T/T_{ref})^{3/2}\frac{T_{ref}+110.4}{T+110.4} \tag{6}$$

For air, $\mu_{ref}=1.71\times10^{-5}kg/(m\cdot s)$ at $T_{ref}=273K$. The constant thermal conductivity κ is chosen to keep Prandtl number $Pr=0.89$ in which the μ is computed at $T=293K$ using Eq.(6). The computed flowfield outside the initial energy deposition region was found to be insensitive to the Rosseland mean absorption coefficient α_R ranging from 1 m^{-1} to 1,000,000 m^{-1}.

The Flux-Corrected Transport algorithm [10] is used and the second order Godunov method is applied to compute the inviscid fluxes. The two-stage Runge-Kutta method is utilized for the time integration. The first and second order MUSCL scheme [11] is used for the reconstruction of the flow variables at the interfaces of the adjacent cells. The algorithm is second order accurate in space and time.

For both the one-dimensional and three-dimensional simulations, a spherically symmetric initial temperature distribution is proposed to model the laser energy pulse assuming the energy is added instantaneously at constant volume (therefore the density is constant) and the gas is ideal. The temperature variation using a Gaussian profile can be written as

$$\Delta T=\Delta T_0 e^{-r^2/r_0^2} \tag{7}$$

where ΔT_0, the peak temperature variation is determined by the total energy deposited

$$\epsilon_E E=\int_0^{2\pi}\int_0^{\pi}\int_0^{\infty} r^2\sin\theta\rho_\infty c_v\Delta T dr d\theta d\phi \tag{8}$$

where E is the energy of the incident laser pulse and c_v is the specific heat at constant volume. Substituting (7) into the above equation and integrating it, we obtain

$$\Delta T_0=\frac{\epsilon_E E}{\pi^{3/2}{r_0}^3\rho_\infty c_v} \tag{9}$$

where r_0 is related to the initial radius R_0=0.90 mm of the laser spot obtained from the laser perturbation focal volume $V_0=\frac{4}{3}\pi R_0^3$ and set to be $R_0/2$. From Eq. (7), ΔT will reach 2% of ΔT_0 at $r=R_0$.

The second model incorporates detailed gas chemistry with an eleven species model (N_2, O_2, NO, N, O, N_2^+, O_2^+, NO^+, N^+, O^+, e), finite-rate ionization of the gas in the focal region by the cascade release of electrons (inverse bremsstrahlung), and the absorption and reflection of laser energy by the plasma. Model details are presented in Kandala and Candler [12]. We faced two major challenges in the development of this model. First, the absorption and reflection parameters for laser energy

deposition are not known in general, and therefore preliminary parameter studies were performed to ascertain appropriate values by comparison with our experimental data. Second, the simulations of laser energy deposition are extraordinarily time-consuming, since the characteristic time scales of ionization and electron energy redistribution are on the order of 10^{-15} sec while the convective flow time scales are on the order of 10^{-5} sec. Significant improvement in computational efficiency was achieved through implementation of an implicit time-accurate solver; however, additional reductions in computational cost are achievable. Results of this model are described in Section 3.1. In particular, we observed that over half of the energy deposited by the laser goes into chemical energy, and that a significant time is required for this energy to be released to the flow, resulting in substantial changes to the gas dynamics.

The governing equations are

$$\frac{\partial \rho_s}{\partial t} + \frac{\partial \rho_s u_j}{\partial x_j} = -\frac{\partial \rho_s v_{s_j}}{\partial x_j} + w_s \tag{10}$$

$$\frac{\partial \rho u_i}{\partial t} + \frac{\partial \rho u_i u_j}{\partial x_j} = -\frac{\partial p}{\partial x_i} + \frac{\partial \tau_{ij}}{\partial x_j} \tag{11}$$

$$\frac{\partial E_e}{\partial t} + \frac{\partial \left(E_e + p_e\right)\left(u_j + v_{s_j}\right)}{\partial x_j} = -\frac{\partial q_{e_j}}{\partial x_j} - Q_{h-e} - Q_{v-e} + Q_r + w_e e_e \tag{12}$$

$$\frac{\partial E_v}{\partial t} + \frac{\partial E_v u_j}{\partial x_j} = -\frac{\partial q_{v_j}}{\partial x_j} - \frac{\partial}{\partial x_j}\sum_{s=1}^{n} v_{s_j} E_{v,s} + Q_{T-v} + Q_{e-v} + \sum_{s=1}^{n} w_s e_{v,s} \tag{13}$$

$$\frac{\partial E}{\partial t} + \frac{\partial \left(E + p\right) u_j}{\partial x_j} = -\frac{\partial}{\partial x_j}\left(q_j + q_{v_j} + q_{e_j}\right) - \frac{\partial u_i \tau_{ij}}{\partial x_j} - \frac{\partial}{\partial x_j}\sum_{s=1}^{n} v_{s_j} \rho_s h_s + Q_r \tag{14}$$

These equations represent the conservation of mass, momentum, electron energy, vibrational energy and total energy, respectively, The subscript $_s$ denotes a species, u_i is the mass-averaged velocity, v_{s_i} is the species diffusive velocity, and w_s is the rate of production of species s. The viscous stress tensor is denoted by τ_{ij} and a Newtonian viscosity law is assumed. The static pressure of the gas is p. The electron energy per unit volume is E_e and p_e is the electron pressure. The conductive flux of electron energy q_{e_j} is given by Fourier's Law with the thermal conductivity of electrons from Mitchner and Kruger [13]. Additional details are presented in Kandala and Candler [14].

2.3 Experimental Facilities

Experiments (except laser energy deposition in quiescent air) were performed in the Mach 3.45 supersonic wind tunnel of the Rutgers Gas Dynamics and Laser Diagnostics Laboratory. The tunnel is a blow-down facility with compressed air supplied from high pressure (16.6 MPa) air storage tanks with a capacity of 8 m^3. Three four-stage compressors and a regenerative air dryer are employed. The test section is 15.2 cm $\times$ 15.2 cm, and the total available test time is several minutes per day. Test section stagnation pressure can be set in the range of 0.55 to 4.8 MPa, with a typical value of 1.0 MPa, and the stagnation temperature is ambient (typically 290 K). The Reynolds number per meter is $1.5 - 24.0 \times 10^7$.

3 Results

3.1 Energy Deposition in Quiescent Air

Perfect Gas Model

The ambient condition is temperature T_∞=293 K, density $\rho_\infty = 1.20$ kg/m^3 and freestream velocity $\vec{U}_\infty = 0$, which is consistent with the experiment. The initial laser spot radius is R_0=0.90 mm. Two different grid spacings (Δr=0.01 mm and 0.02 mm) are used and show 1.3% difference in predicting the profile of shock wave radius *vs* time in Fig. 6, showing the grid resolution in the simulation is sufficient. The grid spacing of Δr=0.01 mm was therefore used in all the simulations.

A blast wave formed by the rapid expansion of the high pressure and temperature region propagates into the ambient air. The position of the leading front varying with time for E=112 mJ is shown in Fig. 6. The position of the blast front is determined by locating the maximum pressure along the radial distance from the center of the source. Considering not all of the laser energy is absorbed and some of the energy is reflected, transmitted, scattered and emitted by the plasma, the total energy absorbed is assumed to be $\epsilon_E E$. Therefore,

$$\Delta T_0 = \frac{\epsilon_E E}{\pi^{3/2} r_0{}^3 \rho_\infty c_v} \qquad (15)$$

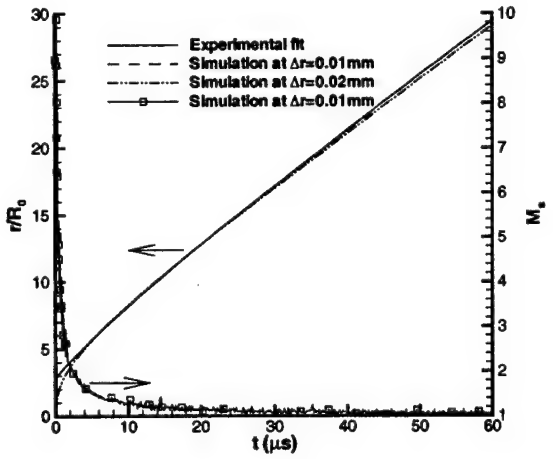

Figure 6: Shock wave radius and shock Mach number *vs* time for E =112 mJ

The net energy deposited ($\epsilon_E E$) in the flow affects the flow characteristics. The choice of ϵ_E is based on the criterion that the standard deviation of the predicted profile of the shock wave radius *vs* time is within 5% of the experimental fit. The results using $\epsilon_E = 0.65$ show good agreement with experimental fit given in Adelgren [15] for E=112 mJ ($r(t) = 140.692\ t^{0.893} + 2.466 \times 10^{-3}$, where t is in seconds and r in meters) except at very early time instants ($t < 5\mu s$) where no experimental data are available. The experimental fit of Adelgren agrees with experiment to within $\pm$5% for $t = 5\ \mu s$ to 40 μs.

Taylor [16] and Sedov [17] proposed a similarity law at the early stage of the air explosion, $r(t) = At^{0.4}$ where A is the function of input energy and ambient density when $M_s^2 \gg 1$ (where $M_s = V_s/a_\infty$, and M_s, V_s and a_∞ are the shock Mach number, shock velocity and ambient speed of sound, respectively.) Jiang *et al* [18] utilized this law as the initial condition and they found that the flow showed non self-simlar behavior in the mid and far-field regimes where the shock is too weak to follow Taylor's similarity law.

The different behavior in our study compared to Taylor's similarity law is due to the relative weak strength of the shock wave in our case, which is demonstrated in Fig. 6 showing that the Mach number at $t = 5\mu s$, which is the first time record in our experiment, is about 1.6 and that the shock strength decreases rapidly until it propagates at essentially the speed of sound.

Figs. 7, 8, 9 and 10 show the experimental contour plots for E=145 mJ at $t = 20\mu s$. The laser beam is incident from the left. The origin (0,0) in (x, y) plane is the center of the laser spot. For

the velocity contours, only the magnitude of the y component is shown. In the experiment, the temperature and pressure were measured and the density was computed from the equation of state for perfect gas. The experimental uncertainty in the measurement of the pressure, temperature and velocity is $\pm 2\%$, $\pm 1\%$ and $\pm 4\%$, respectively. The central part is blanked out since no experimental data are available there. In the incident direction, the blast wave shows a asymmetric shape due to the directional formation of the plasma, while in the vertical direction, the shape is fairly symmetric and the data is extracted in this direction to compare with the simulation.

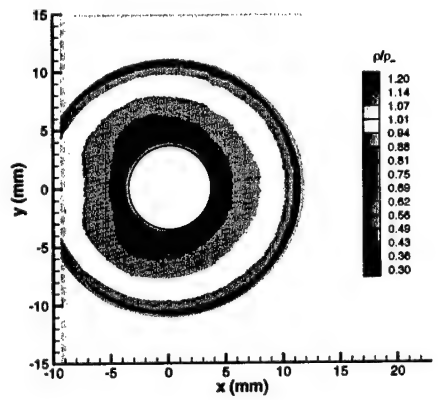

Figure 7: Density contours at $t = 20\mu s$ for E =145 mJ

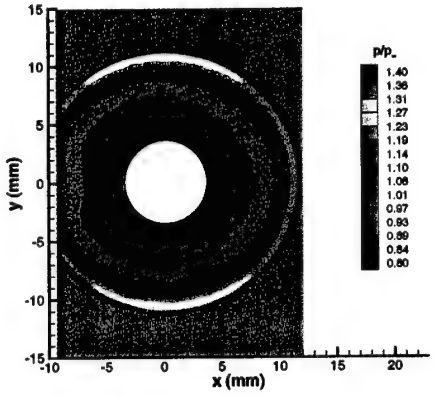

Figure 8: Pressure contours at $t = 20\mu s$ for E =145 mJ

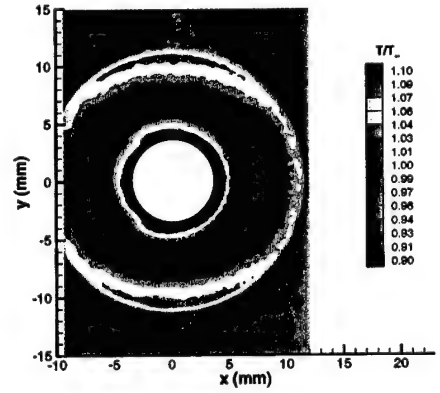

Figure 9: Temperature contours at $t = 20\mu s$ for E =145 mJ

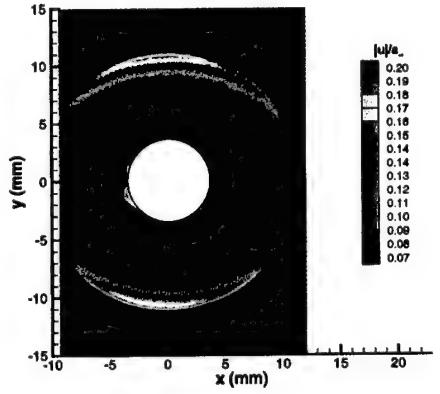

Figure 10: Velocity contours at $t = 20\mu s$ for E =145 mJ

Figs. 11, 12, 13 and 14 show the comparison with experiment at $t = 20\mu s$ for E=145mJ. The experimental data is extracted along a vertical line from y=0 mm to y=15 mm. The assumed absorption coefficient is $\epsilon_E = 0.5$. Good agreement is achieved for the shock wave position, the magnitude of the change of the flow variables across the shock and the distribution of flow variables for points with r less than the shock radius and outside the laser spot region. Since the intensity of Rayleigh Scattering (RS) is proportional to the density and the density is very low at the center of the energy spot, the uncertainty increases near the center due to lower signal levels in RS. Also as

mentioned previously, the RS is dominated by the plasma emission for early time so no experimental information is shown here.

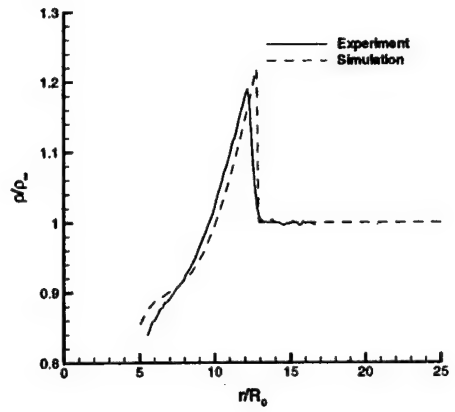

Figure 11: Density *vs* radius at $t = 20\mu s$ for E =145 mJ

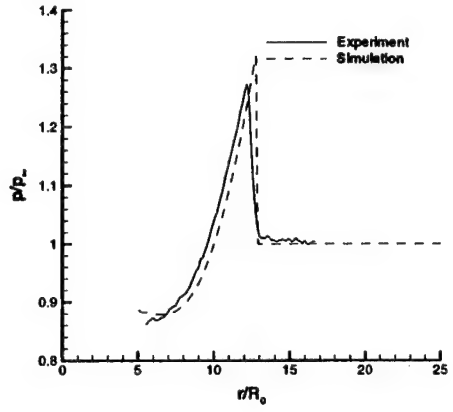

Figure 12: Pressure *vs* radius at $t = 20\mu s$ for E =145 mJ

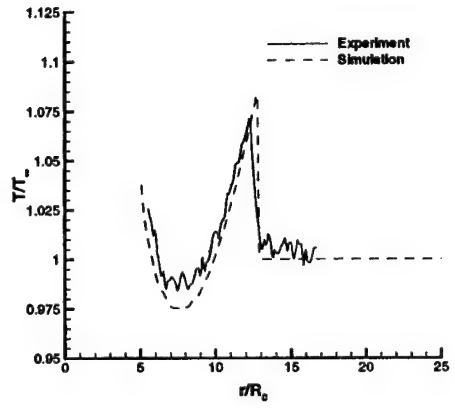

Figure 13: Temperature *vs* radius at $t = 20\mu s$ for E =145 mJ

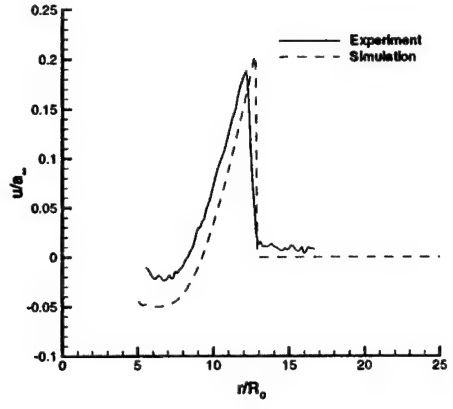

Figure 14: Velocity *vs* radius at $t = 20\mu s$ for E =145 mJ

Real Gas Model

The real gas model describes the laser energy deposition and subsequent flow evolution by the Navier-Stokes equations with extension to include nonequilibrium thermochemistry and radiative transport. Air is modeled using eleven chemical species (N2, O2, NO, N, O, N2+, O2+, NO+,N+, O+, e).

The absorption and reflection parameters of the model were calibrated by comparison with the experimental data for shock radius *vs* time. Fig. 15 displays the close agreement between computed and experimental shock radius *vs* time for a Nd:YAG laser pulse (108 mJ, 20 ns) in air at STP. The computed and experimental static pressure, static temperature and horizontal velocity on the symmetry plane are displayed in Figs. 16, 17, 18, respectively. Generally good agreement is observed in the region of measurement.

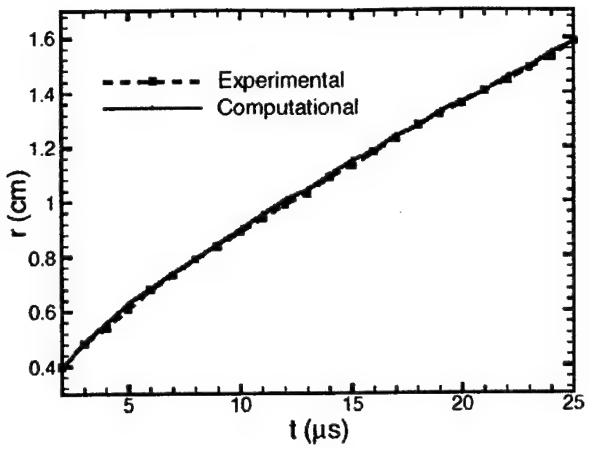

Figure 15: Shock radius *vs* time for E =145 mJ

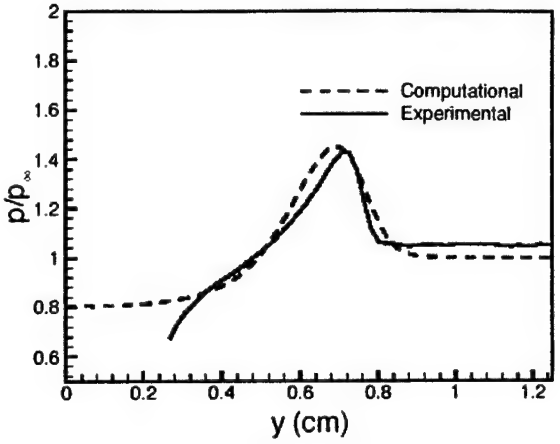

Figure 16: Static pressure at $t = 10\mu s$ for E =145 mJ

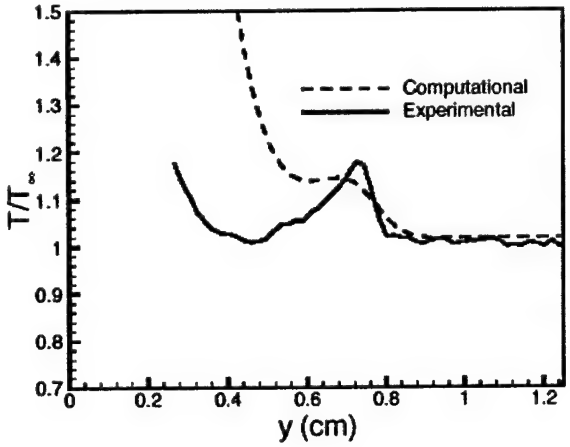

Figure 17: Static temperature at $t = 10\mu s$ for E =145 mJ

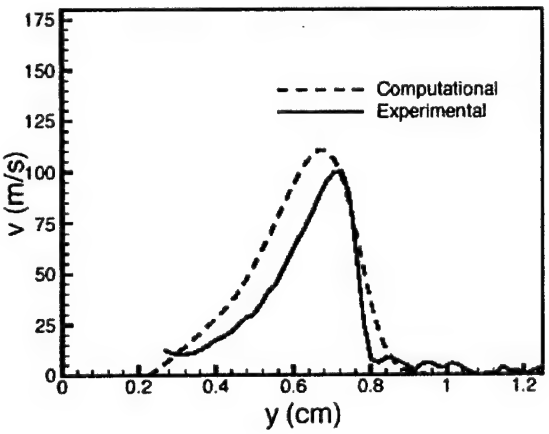

Figure 18: Velocity at $t = 10\mu s$ for E =145 mJ

3.2 Laser Energy Deposition Upstream of an Edney IV Interaction

The Edney IV interaction [19] causes intense surface heat transfer due to the impingement of a supersonic jet, formed by the interaction of a blunt body shock and a separate incident shock, with the surface (Fig. 19). The peak heat transfer can be several orders of magnitude above the ordinary stagnation heat transfer of the isolated body. Analysis of the National AeroSpace Plane indicated that an Edney IV interaction on the inlet cowl could result in a heat transfer rate of 1.2×10^9 W/m^2, equivalent to delivering the entire power output of a moderate size nuclear power plant to a 1 m^2 surface.

A hypersonic aircraft would be designed to operate outside of the conditions which lead to an Edney IV interaction. The five other types of shock-shock interactions (Fig. 20) result in significantly lower surface heat transfer than the Edney IV interaction. Nevertheless, the aircraft might momentarily enter a flight attitude due to vehicle maneuver or gust response wherein the Edney IV interaction would occur. Therefore, a flow control technique for alleviating or eliminating

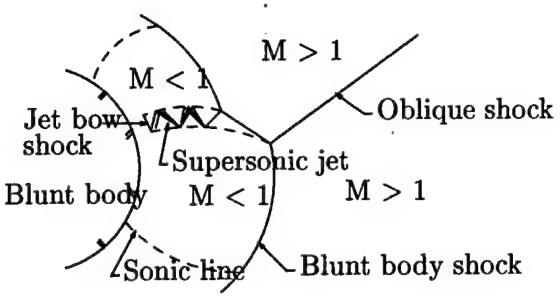

Figure 19: Edney IV interaction

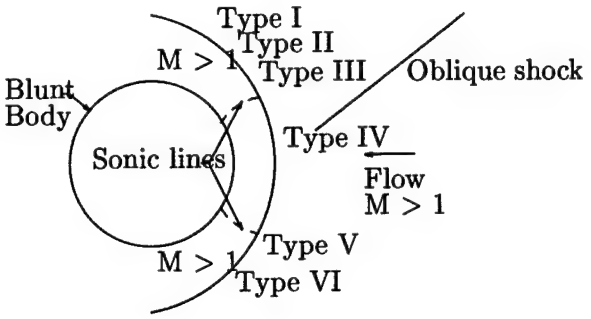

Figure 20: Edney I-VI interactions

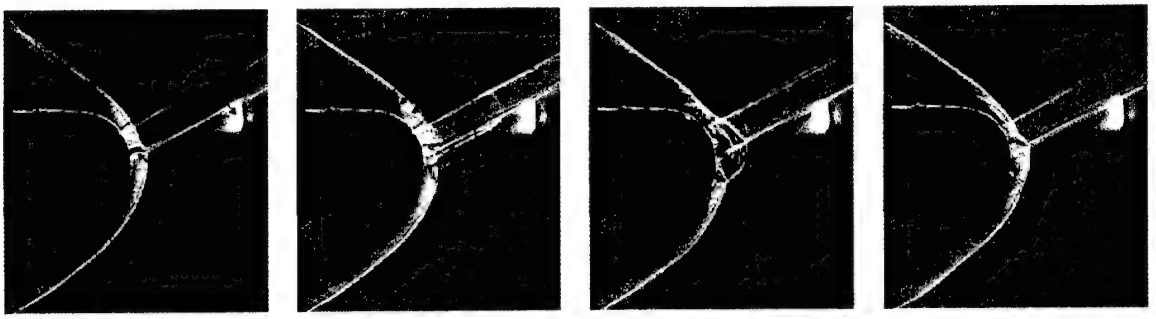

(a) t=0 μs (b) t=40 μs (c) t=80 μs (d) t=110 μs

Figure 21: Schlieren image of Edney IV interaction (E=293 mJ)

the Edney IV interaction is needed.

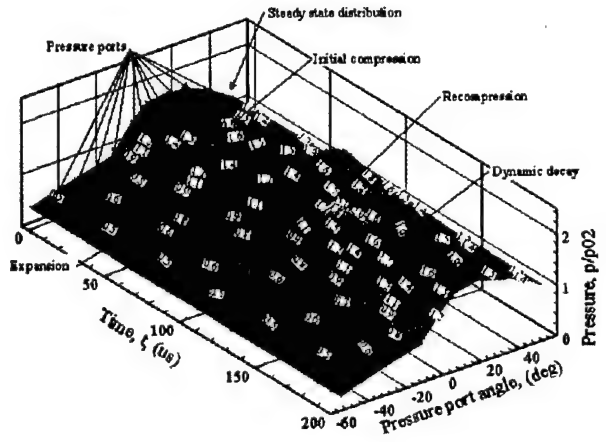

Figure 22: Surface pressure *vs* time

An experimental study was conducted at $M_\infty = 3.45$ to assess the capability of laser energy deposition to reduce the peak aerothermodynamic loads due to an Edney IV interaction generated by the interaction of an oblique shock wave, generated by a 15° wedge, with a 25.4 mm sphere. The stagnation pressure p_{t_∞} and temperature T_{t_∞} are 1.138 MPa and 283 K, respectively. High frequency surface pressure measurements were obtained on the centerplane of the sphere for angles $-55° \leq \theta \leq 51°$. Preliminary surface heat transfer measurements were also performed [7].

Schlieren images of laser energy deposition ($E = 293$ mJ) are shown in Fig. 21. Fig. 21(a) shows the Edney IV interaction (The upper oblique wave in the schlieren image is a weak Mach wave near the tunnel sidewall and does not interfere with the Edney IV interaction. The impinging shock wave is the lower oblique wave.) including the impinging supersonic jet and the location of the laser pulse (*i.e.*, the bright spot). Fig. 21(b) shows the blast wave and plasma region interacting with the oblique and blunt body shocks. Fig. 21(c) indicates the substantial modification of the Edney IV

shock structure due to the interaction with the plasma region; in particular, the supersonic jet has been completely disrupted. Fig. 21(d) indicates the restoration of the Edney IV interaction following the passage of the plasma region.

The laser pulse causes a significant reduction is surface pressure. Fig.22 displays the experimental surface pressure for $-55° \leq \theta \leq 51°$. An initial small compression is caused by the impact of the blast wave with the surface. The subsequent interaction of the high temperature plasma region with the shock structure deflects the supersonic jet and generates an expansion wave [6]. These two effects cause a reduction in the surface pressure. These results, while not conclusive evidence of the capability for reducing peak heat transfer associated with Edney IV interactions, are nevertheless suggestive that energy deposition is a promising candidate for control of this critically important phenomena.

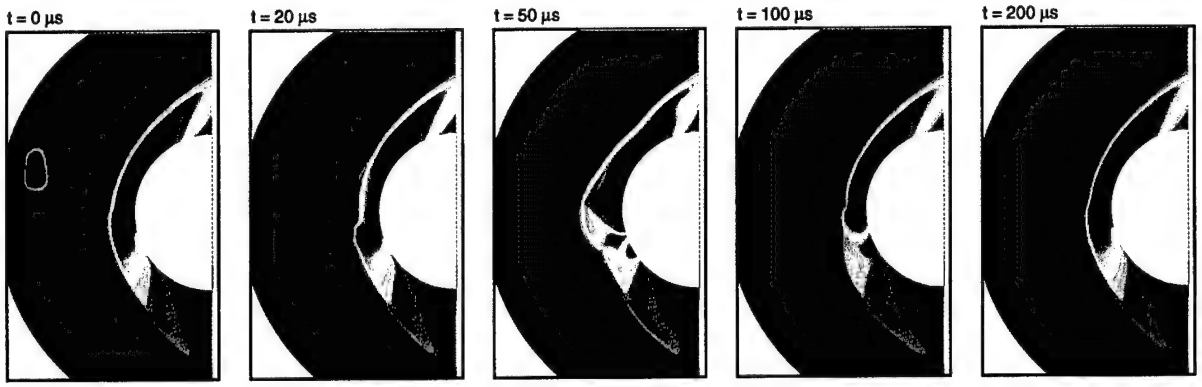

(a) t=0 μs (b) t=20 μs (c) t=50 μs (d) t=100 μs (e) t=200 μs

Figure 23: Pressure contours for laser energy deposition upstream of Edney Type IV Interaction

A series of 3-D simulations were performed using the real gas model to study the effect of energy deposition in a steady supersonic flow with an Edney Type IV shock-shock interaction. Energy from a laser discharge was deposited upstream of the Edney Type IV interaction in a steady supersonic flow. The flow conditions were set to simulate the experiments done at Rutgers University [20]. As the energy deposition region interacts with the shock structures in front of the sphere, there is a substantial decrease in the peak pressures on the surface of the sphere. This reduction of pressure varies with the location of energy deposition region. By varying the location, the pressure reduction can be maximized. Fig. 23 shows the pressure contours for the energy deposition. It was also found that the energy deposition region has a large amount of chemical energy due to air dissociation. As the gas cools, the dissociated species recombine through exothermic reactions, leading to a delayed release of energy and sustaining the effect of laser energy deposition region over a longer time. During the energy absorption process a number of chemical reactions take place. The rates of these reactions can be very high, imposing a stiff penalty on the time-step in explicit computation. Direct linearization of these source terms will not improve the time-step. This is because the source term consists of production and destruction terms, each of which depends in different ways on the conserved variables. Instead, we use a linearization scheme developed by Spalart and Allmaras that handles the linearization of these production and destruction terms separately. A time-step increase of the order of 1000 can be achieved.

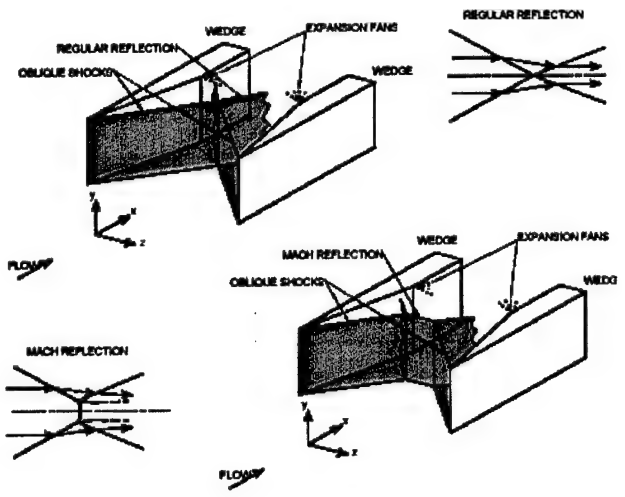

Figure 24: MR and RR

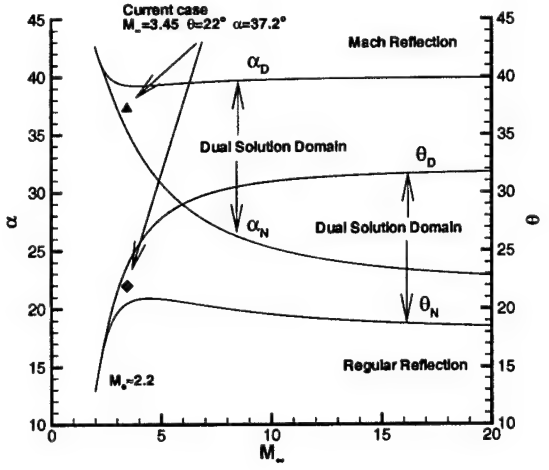

Figure 25: Dual solution domain

In addition to the Edney IV experiments described above, a series of experiments [7, 6]and simulations [14] for energy deposition upstream of an isolated sphere at $M_\infty = 3.45$ were performed. These experiments and simulations also demonstrated the capability for momentary reduction in surface pressure by laser energy deposition. A detailed discussion is presented in Adelgren *et al* [6] and Adelgren [7] including a theoretical analysis of the effect of the interaction of a temperature discontinuity with a normal shock which illustrates the reduction in surface pressure due the formation of an expansion wave.

3.3 Control of Mach Reflection to Regular Reflection in Dual Solution Domain

The crossing shock wave interaction is a fundamental phenomenon in high speed flight. For example, a scramjet powered hypersonic vehicle may utilize shock interactions to decelerate the flowfield in the inlets for more efficient combustion. The intersection of two symmetric oblique shock waves may result in either an RR or an MR (Fig. 24). When the incoming Mach number (M_∞) exceeds a critical Mach number M_C (where M_C is 2.202 for a diatomic gas ([21]) and is approximately 2.2 for perfect air), a Dual Solution Domain (DSD) is formed, wherein either an RR or an MR can theoretically exist shown in Fig. 25. The total pressure loss across the normal shock in a MR is substantially greater than across the RR, and therefore a scramjet inlet would be designed to operate with the RR domain. Nevertheless, the inlet flowfield may momentarily enter the DSD due to vehicle maneuver or gust response, and therefore a flow control technique for forcing a MR to RR transition in the DSD is essential.

A detailed 3-D simulation of laser energy deposition upstream of a MR formed by symmetric shock waves generated by 22° wedges at Mach 3.45 was performed. The flow conditions correspond to the experiments performed at Rutgers University (Adelgren et al [6]).

A Mach 3.45 flow enters two symmetric 22° wedges, which corresponds to a point midway in the DSD shown in Fig. 25. Once an MR is formed, a single laser pulse (E =215 mJ) is added above the horizontal center plane and on the vertical center plane shown in the numerical model (Fig. 26).

The computational domain $L_x \times L_y \times L_z$ shown in Fig. 26 is $3.5w \times 4w \times 2.2w$, where $w = 25.4$ mm

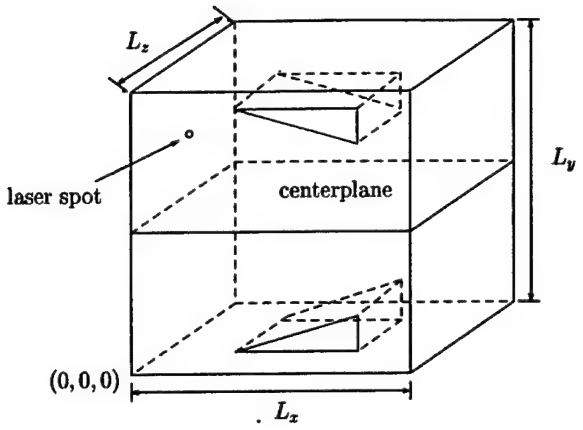

Figure 26: Computational domain

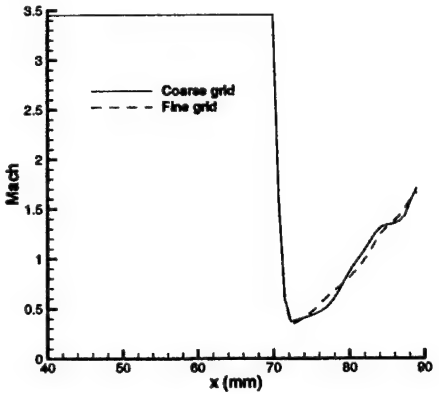

Figure 27: Mach number along centerline

is the shock generator length measured along wedge surface. The $x = 0$, $y = 0$ and $z = 0$ planes are the inflow boundary, the lower boundary and the vertical centerplane, respectively. The streamwise length L_x was chosen to insure supersonic flow at the downstream boundary and to keep the blast wave from the laser pulse away from the upstream boundary. The transverse and spanwise lengths L_y and L_z are based on the requirement that the reflections at the boundaries of the acoustic disturbances originating from the tip of the wedge and the blast waves from the laser pulse do not interact with the flow structure in the vicinity of the Mach stem. The trailing edges of the two wedges are placed $2.5w$ downstream of the inflow. The center of the laser spot is located at $0.2w$ downstream of the leading edge and $0.9w$ above the horizontal center plane in accordance with the experiment.

The flow solver is GASPex which solves the compressible Euler equations. The third-order accurate Van Leer scheme along with Mid-Mod limiter is used to compute the inviscid fluxes in each direction and a two-stage Runge-Kutta scheme is used for the time integration.

The inflow boundary is a uniform Mach 3.45 flowfield and the extrapolation technique is used for the outflow. The symmetric boundary is used for the $z = 0$ plane. The slip boundary condition is utilized on the wedge surfaces and also on the upper and lower boundary and $z = L_z$ plane for simulating the wind tunnel side walls.

The grid is generated by a commercial software ICEMCFD. Two sets of grids are generated to conduct a grid refinement study. Approximately 11 to 25 layers of cells are used to resolve the Mach stem in the vertical direction for the coarse and fine grids, respectively. The total number of cells are 1.5 million and 5.0 million for the coarse and fine grids, respectively. The grid convergency is demonstrated in Fig. 27.

The computation is performed in two steps. The flowfield is first converged to a steady state in the absence of any laser perturbation. Then, a single Nd:YAG laser pulse of 215 mJ was focused upstream of the shock and above the symmetry plane.

The steady flow structure without the energy perturbation is first shown. The steady state is obtained when the Mach stem location doesn't change with time at the vertical centerplane. Fig. 28 demonstrates the flow structures at the $z = 0$ plane for the fine grid. Two oblique shock waves generated by the leading edges form a Mach reflection. The flow after this normal shock becomes subsonic. The expansion fans emanating from the trailing edges are refracted through the reflected

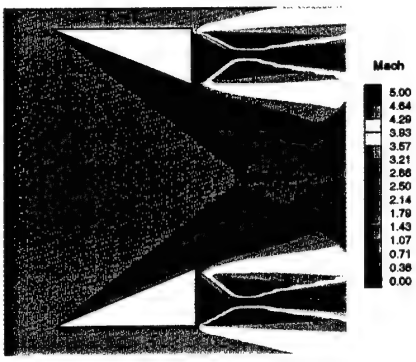

Figure 28: Mach number contours at vertical centerplane

Figure 29: Density isosurface for MR

shocks and interact with slipstreams, forming a converging-diverging nozzle to accelerate the flow to be supersonic. The Kelvin-Helmholtz structures are clearly observed propagating along the sliplines, due to the difference in both the velocity and the density along the sliplines. The predicted spanwise averaged Mach stem height is 1.96 mm for the coarse and fine grid, and it is within 2% of the experimental value of 2 mm. The measurement uncertainty of the Mach stem height is $\pm 10\%$. All the following computational results are shown for the fine grid simulation.

Three dimensional effects, due to the finite aspect ratio of the wedges, are seen in the spanwise variation of the Mach stem height. Fig. 29 shows this variation in a plot of the isosurface of density for $\rho/\rho_\infty = 3.57$. The Mach stem decreases in height from the centerplane (which corresponds to the right edge in the figure) and disappears close to the edge of the wedge (which corresponds to the left edge in the figure). This observation is consistent with the study by Ivanov *et al*[22].

Once the steady MR is formed, a laser pulse is added. The experimental schlieren images are shown in Figs. 30 in which each experimental schlieren image is an ensemble of three to eight experiments, although the instantaneous images show the same trends as described below. The numerical schlieren images which are the contour plot of the first derivative of the density along the streamwise direction at the $z = 0$ plane are plotted for qualitative comparison in Figs. 31.

Figs. 30(a) to 30(b) and Figs. 31(a) to 31(b) show the process of the blast wave and the thermal spot interacting with the upper oblique shock wave, causing an upstream deflection of the oblique shock due to the lowering of the local Mach number from the thermal spot. This deflection eventually reaches the Mach stem (Figs. 30(c) and 31(c)) at approximately $t = 60\mu s$ causing a reduction in the height of the Mach stem. In the experiment, the Mach stem decreases monotonically to 30% of its original height as shown in Fig. 32. This return to an MR may be due to freestream disturbances in the tunnel. The simulation shows that the Mach stem finally disappears along the entire wedge span as shown in Fig. 33 and Fig. 34 and a complete transition of MR to RR is achieved. The computation runs for 2.0 flowthrough times following the establishment of the RR (where, one flowthrough time is defined as the time for the freestream to traverse the whole computational domain) and the RR is stable as shown in Fig. 34 (where $t = 280\mu s$ is the limit of the computation).

The transition from an MR to an RR may be described as follows. As mentioned above, the thermal spot and its induced blast wave convect with the freestream, and first intersect with the upper

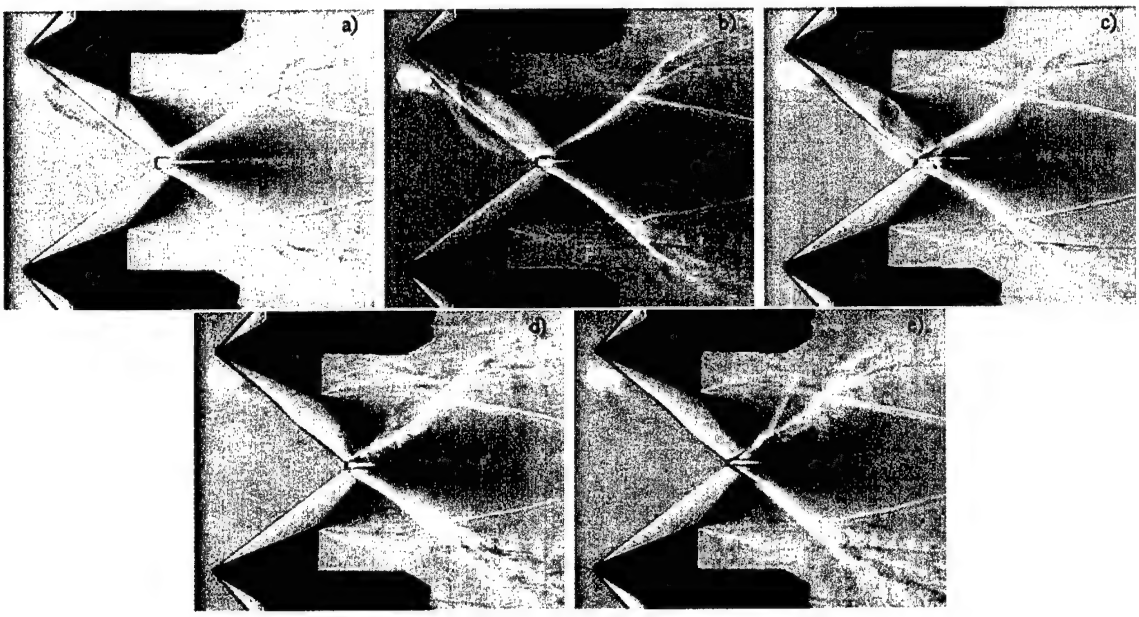

Figure 30: Experiment, a) $t = 20\ \mu s$, b) $t = 40\ \mu s$, c) $t = 60\ \mu s$, d) $t = 80\ \mu s$, e) $t = 100\ \mu s$

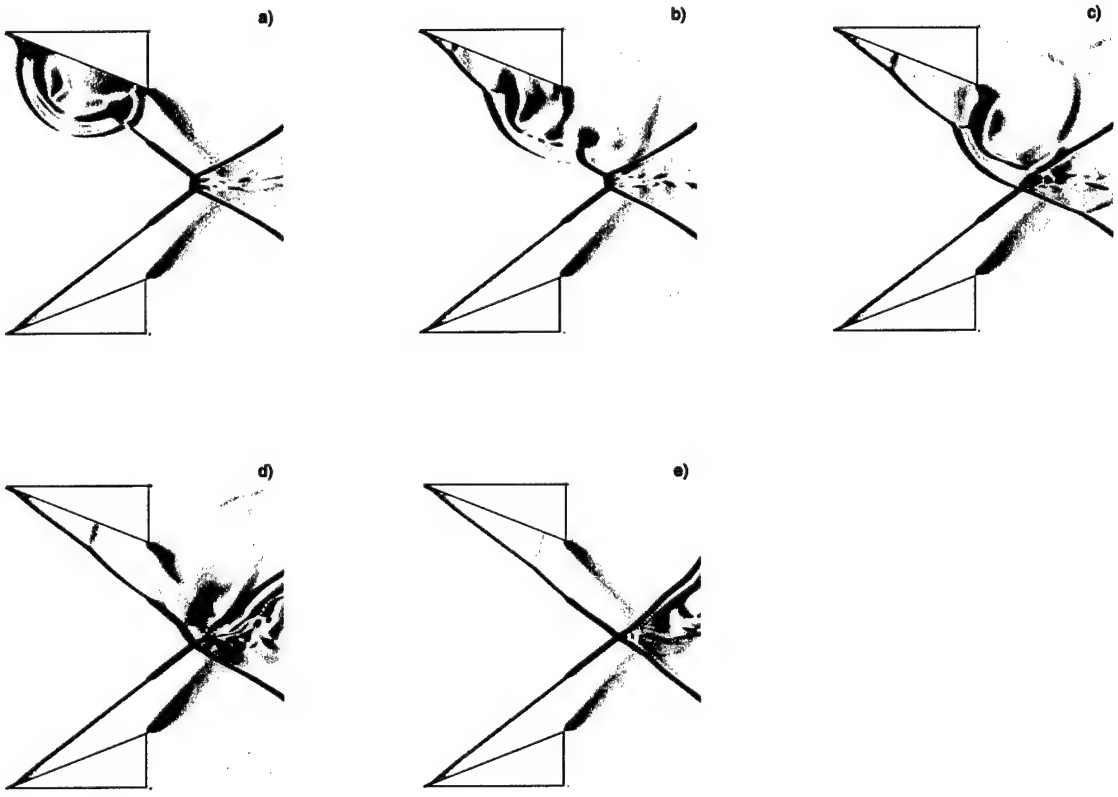

Figure 31: Simulation, see Fig. 8 for legend.

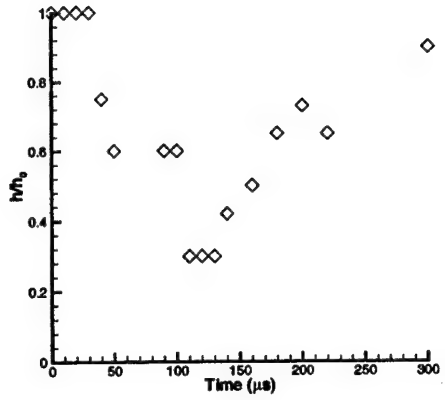

Figure 32: Mach stem height *vs* x

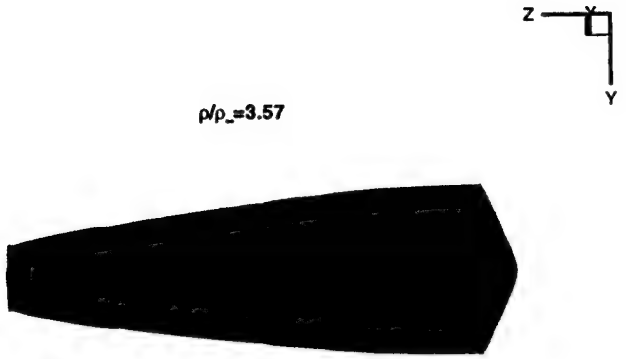

Figure 33: Density isosurface at $t = 280\mu s$

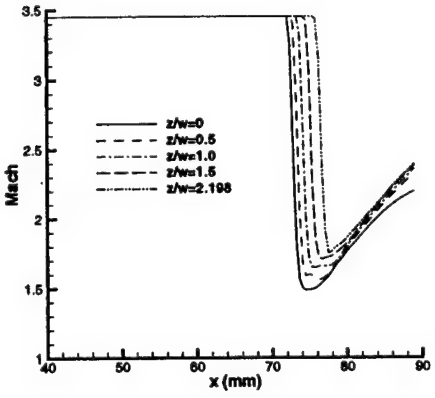

Figure 34: Mach stem height *vs* t in experiment

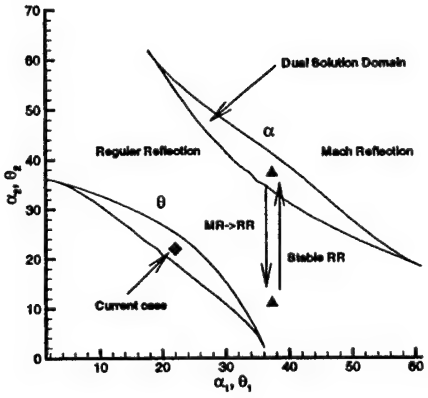

Figure 35: (α_1, α_2) plane and (θ_1, θ_2) plane for M_∞=3.45

oblique shock. Their intersections generate a complicated shock system, including the reflection of the blast wave and expansion waves on the wedge surface, and the deflection and lensing of the upper oblique shock ([7]). As the deflected upper oblique shock reaches the Mach stem, the local shock angle is smaller than that for the lower oblique shock, therefore these symmetric double wedges actually act as two asymmetric wedges. Fig. 25 shown for symmetric double wedges is not suitable to explain the transition any more. [23] and [24] demonstrated that a hysteresis phenomenon existed in the reflection of asymmetric shock waves. Following this idea, we consider that the asymmetric laser pulse may affect the shock reflection from the symmetric reflection to the asymmetric reflection. Fig. 35 shows the DSD in (θ_1, θ_2) plane for $M_\infty = 3.45$, where θ_1 and θ_2 denote the lower and upper wedge angle, respectively. The initial wedge angle is displayed by a diamond symbol in the middle of the DSD, and it is also plotted in (α_1, α_2) plane in Fig. 35, where α_1 and α_2 denote the lower and upper oblique shock angle, respectively. The MR $\rightarrow$ RR transition is described in Fig. 35. As the deflected upper oblique shock reaches the Mach stem, the local shock angle is decreased to approximately 11° as shown in Fig. 31(c), while the lower oblique shock angle remains almost unchanged (37.3°). The initial point in the DSD moves below the von Neumann angle, wherein only an RR exists. When the thermal effects passes the Mach stem, the upper oblique shock angle changes back to its initial value into the DSD. However, the RR remains stable unless the shock angle reaches the detachment angle [25].

4 Personnel

The personnel of the research project are listed in Table 1.

Table 1: Personnel

Name	Title	Period of Participation	Supported by
Prof. Doyle Knight	Principal Investigator	June 01 - November 03	this grant
Prof. Greg Elliott		June 01 - November 03	this grant
Prof. Graham Candler		June 01 - November 03	this grant
Dr. Alexander Zheltovodov		June 01 - November 03	Rutgers University
Dr. Hong Yan		June 01 - November 03	this grant
Major Russell Adelgren		June 01 - Sept 02	AFIT
Mr. Ramnath Kandala		June 01 - November 03	this grant

5 Publications

5.1 Journal Publications

Yan, H., Adelgren, R., Elliott, G., Boguszko, M., and Knight, D., "Laser Energy Deposition in Quiescent Air", AIAA J. Vol. 41, No. 10, pp.1988-1995, 2003.

Yan, H., Adelgren, R., Elliott, G., Knight, D., and Beutner, T., "Laser Energy Deposition in Intersecting Shocks", Shock Waves, Vol. 13, pp.113-121, 2003.

5.2 Conference Publications

Adelgren, R., Elliott, G., Knight, D., Zheltovodov, A., and Buetner, T., "Energy Deposition in Supersonic Flows", AIAA Paper No. 2001-0885, January 2001.

Adelgren, R., Elliott, G., Knight, D., Zheltovodov, A., and Buetner, T., "Localized Flow Control in Supersonic Flows by Pulsed Laser Energy Deposition", Third Workshop on Magneto- and Plasma Aerodynamics for Aerospace Applications, IVTAN, Moscow, Russia, April 2001.

Adelgren, R., Elliott, G., Knight, D., Buetner, T., Ivanov, M., and Zheltovodov, A., "Laser Energy Deposition in Transverse Wall Jets and Intersecting Shocks", Workshop on Thermochemical Processes in Plasma Aerodynamics, Hypersonic System Research Institute, St. Petersburg, Russia, September 2001.

Knight, D., Kuchinskiy, V., Kuranov, A., Sheikin, E., "Aerodynamic Flow Control at High Speed Using Energy Deposition", Fourth Workshop on Magneto- and Plasma Aerodynamics for Aerospace Applications, IVTAN, Moscow, Russia, April 2002.

Yan, H., Adelgren, R., Elliott, G., Knight, D., Buetner, T., Ivanov, M., Kudryavtsev, A., and Khotyanovsky, D., "Laser Energy Deposition in Quiescent Air and Intersecting Shocks", Fourth Workshop on Magneto- and Plasma Aerodynamics for Aerospace Applications, IVTAN, Moscow, Russia, April 2002.

Kandala, R., and Candler, G., Computational Modeling of Localized Laser Energy Deposition in Quiescent Air, AIAA Paper No. 2002-2160, May 2002.

Yan, H., Adelgren, R., Elliott, G., Knight, D., Beutner, T., and Ivanov, M., "Laser Energy Deposition in Intersecting Shocks", AIAA Paper No. 2002-2729, June 2002.

Knight, D., Adelgren, R., Elliott, G., and Yan, H., "Local Control of Supersonic Flows Using Laser Energy Deposition", EUROMECH 440, Marseilles, France, September 2002.

Adelgren, R., Yan, H., Elliott, G., Knight, D., Zheltovodov, A., and Ivanov, M., "Localized Flow Control by Laser Energy Deposition Applied to Edney IV and Intersecting Shocks", AIAA Paper No. 2003-0031, January 2003.

Knight, D., Kuchinskiy, V., Kuranov, A., and Sheikin, E., "Survey of Aerodynamic Flow Control at High Speed Using Energy Addition", AIAA Paper No. 2003-0525, January 2003.

Yan, H., Adelgren, R., Elliott, G., Knight, D., Boguszko, M., and Ivanov, M., "Laser Energy Deposition in Quiescent Air", AIAA Paper No. 2003-1051, January 2003.

Kandala, R., Candler, G., Numerical Studies of Laser-Induced Energy Deposition for Supersonic Flow Control, AIAA Paper No. 2003-1052, January 2003.

References

[1] Van Wie, D., White, M., and Corpening, G., "NASP Inlet Design and Testing Issues," *Johns Hopkins APL Technical Digest*, Vol. 11, 1990, pp. 353–362.

[2] Pilyugin, N., Talipov, R., and Khlebnikov, V., "Supersonic Flow over the Bodies by the Flow with Physical-Chemical Heterogeneity," *Thermophysics of High Temperatures*, Vol. 35, 1997, pp. 322–336.

[3] Tretyakov, P., Garanin, A., Kraynev, V., Tupikin, A., and Yakovlev, V., "Investigation of Local Laser Energy Release Influence on Supersonic Flow by Methods of Aerophysical Experiments," *International Conference on Methods of Aerophysical Research, Novosibirsk, Russia,*, 1996.

[4] Levin, V. and Terent'eva, L., "Supersonic Flow Over a Cone with Heat Release in the Neighborhood of the Apex," *Mekhanika Zhidkosti i Gaza*, , No. 2, 1993, pp. 110–114.

[5] Riggins, D., Nelson, H., and Johnson, E., "Blunt Body Wave Drag Reduction Using Focused Energy Deposition," *AIAA J.*, Vol. 37, No. 4, 1999, pp. 460–467.

[6] Adelgren, R., Yan, H., Elliott, G., Knight, D., Beutner, T., Zheltovodov, A., Ivanov, M., and Khotyanovsky, D., "Localized Flow Control by Laser Energy Deposition Applied to Edney IV Shock Impingement and Intersecting Shocks," *AIAA Paper No. 2003-0031*, 2003.

[7] Adelgren, R., "Localized Flow Control with Energy Deposition," *Ph.D dissertation, Dept of Mechanical and Aerospace Engineering, Rutgers University, September*, 2002.

[8] *www.aerosft.com.*

[9] Yan, H., Adelgren, R., Boguszko, M., Elliott, G., and Knight, D., "Laser Energy Deposition in Quiescent Air," *AIAA J.*, Vol. 11, 2003, pp. 1988–1995.

[10] Boris, J. P. and Book, D. L., "Flux Corrected Transport: I, SHASTA, a Fluid Transport Algorithm that Works," *J. Computational Physics*, Vol. 11, 1973, pp. 38–69.

[11] Van Leer, B., "Towards the Ultimate Conservative Difference Scheme. V. A Second Order Sequel to Godunov's Method," *J. Computational Physics*, Vol. 32, 1979, pp. 101–136.

[12] Kandala, R. and Candler, G., "Computational Modeling of Localized Laser Energy Deposition in Quiescent Air," *AIAA Paper 2002-2160*, 2002.

[13] Mitchner, M. and Kruger, C., *Partially Ionized Gases*, John Wiley and Sons, New York, 1973.

[14] Kandala, R. and Candler, G., "Numerical Studies of Laser-Induced Energy Deposition for Supersonic Flow Control," *AIAA Paper 2003-1052*, 2003.

[15] Adelgren, R., Boguszko, M., and Elliott, G., "Experimental Summary Report – Shock Propagation Measurements for Nd:YAG Laser Induced Breakdown in Quiescent Air," *Dept of Mechanical and Aerospace Engineering, Rutgers University, October*, 2001.

[16] Taylor, G. I., "The Formation of a Blast Wave by a Very Intense Explosion: I Theoretical Discussion," *Proc. Roy. Soc.*, Vol. 201, 1950, pp. 159–174.

[17] Sedov, L. I., *Similarity and Dimensional Methods in Mechanics*, Academic, New York, NY, 1959.

[18] Jiang, Z., Takayama, K., Moosad, K. P. B., Onodera, O., and Sun, M., "Numerical and Experimental Study of a Micro-Blast Wave Generated by Pulsed-Laser Beam Focusing," *Shock Waves*, Vol. 8, 1998, pp. 337–349.

[19] Edney, B., "Anomalous Heat Transfer and Pressure Distribution on Blunt Bodies at Hypersonic Speeds in the Presence of an Impinging Shock," *The Aeronautical Research Institute of Sweden, FAA Report 115*, 1968.

[20] Adelgren, R., Elliott, G., Knight, D., Zheltovodov, A., and Beutner, T., "Energy Deposition in Supersonic Flows," *AIAA Paper No. 2001-0885*, 2001.

[21] Myrabo, L. and Raizer, Y., "Laser-induced Air Spike for Advanced Transatmospheric Vehicles," *AIAA Paper 1994-2451*, 1994.

[22] Ivanov, M., Khotyanovsky, D., Kudryavtsev, A., and Nikiforov, S., "Experimental Study of 3D Shock Wave Configurations During RR $\leftrightarrow$ MR Transition," *23rd International Symposium on Shock Waves*, 2001.

[23] Molder, S., "Particular Conditions for the Termination of Regular Reflection of Shock Waves," *CASI Trans*, Vol. 25, 1979, pp. 44–49.

[24] Ivanov, M., Ben-Dor, G., Elperin, T., Kudryavtsev, A., and Khotyanovsky, D., "The Reflection of Asymmetric Shock Waves in Steady Flows: A numerical investigation," *Journal of Fluid Mechanics*, Vol. 469, 2002, pp. 71–87.

[25] Hornung, H., Oertel, H., and Sandeman, R., "Transition to Mach Reflection of Shock Waves in Steady and Pseudosteady Flow With and Without Relaxation," *J. Fluid Mechanics*, Vol. 90, 1979, pp. 541–560.